

Noncontact AC Voltage Measurements: Error and Noise Analysis

Marcelo Alejandro Haberman^{ID} and Enrique Mario Spinelli

Abstract—A capacitive noncontact ac voltage measurement technique and its feasibility to measure arbitrary waveform signals are analyzed. The method provides self-calibration of the scale factor, an important feature considering the high variability that coupling capacitances present. The analysis of several errors related to the technique is performed, showing the impact of different design parameters on the final accuracy. Scaling errors due to the electronic circuit can be constrained to less than 0.5%, and can be disaffected, whereas those due to the frequency dependence of cable sheath permittivity can be up to 3% for polyvinyl chloride sheathed cables. This error is not controllable by electronic design but requires working on electrode probe. A noise model is also proposed and experimentally validated, showing that signal-to-noise ratios of up to 100 dB are achievable with common components. A functional prototype was built and tested by acquiring power-line voltage and other arbitrary signals without contact. Instantaneous voltage signals were acquired by the proposed technique and contrasted with those acquired directly. For the measurement of power-line voltage and using the self-calibration feature, the instantaneous error was lower than 7 V (2.2%) for a ± 1300 V measurement range at 50 Hz. If manual correction is applied, the error can be reduced to 0.28 V_{rms} (0.12%).

Index Terms—Capacitive sensor, noncontact voltage.

I. INTRODUCTION

CAPACITIVE noncontact voltage measurement (NCVM) techniques facilitate the measurement of dangerous potentials on distribution power-lines [1]–[3], electrostatic charge measurement on distant surfaces [4], [5], and even the acquisition of microvolt level biopotentials [6], [7]. All these techniques are based on capacitive coupling through a small capacitance C_X between a conductor at an unknown potential v_X and a system conductor plate (usually called probe or electrode). There are dc and ac NCVM systems. The dc systems need a variable coupling capacitance to force a current to flow through it [8], while ac systems can be coupled by constant capacitances, resulting in simpler and lower cost systems.

Manuscript received July 22, 2017; revised January 20, 2017; accepted January 22, 2018. Date of publication March 14, 2018; date of current version July 12, 2018. This work was supported in part by the National Scientific and Technical Research Council under Project PIP-0558, in part by La Plata National University under Project I-219, and in part by ANCyT under Project PICT-2015/2257. The Associate Editor coordinating the review process was Dr. Edoardo Fiorucci. (Corresponding author: Marcelo Alejandro Haberman.)

The authors are with the Institute LEICI, UNLP, CONICET, La Plata 1900, Argentina (e-mail: marcelo.haberman@ing.unlp.edu.ar).

Color versions of one or more of the figures in this paper are available online at <http://ieeexplore.ieee.org>.

Digital Object Identifier 10.1109/TIM.2018.2809079

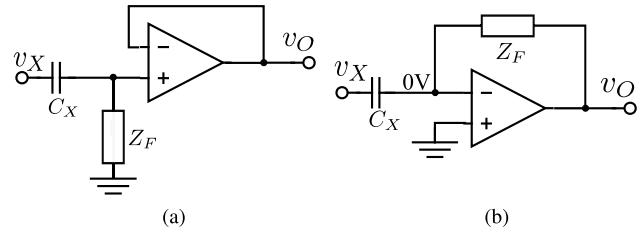


Fig. 1. Typical noncontact measurement topologies. (a) High input impedance. (b) Low input impedance.

Two main circuit topologies are used for NCVM: the high input impedance Z_{in} approach [Fig. 1(a)] and the low Z_{in} topology [Fig. 1(b)]. The first becomes insensitive to C_X when Z_F is high enough (1) and is intended for low-level ac voltages as biopotentials [7], but not for high v_X values because the electronic circuit must cope with potentials close to v_X . On higher voltage applications, such as power-line voltage monitoring [9], [10], Z_F must be low enough to attenuate v_X to a safe input voltage level. The transference function becomes dependent on the coupling capacitance C_X , which must be measured for system calibration

$$V_O(s) = V_X(s) \frac{s \cdot C_X \cdot Z_F}{1 + s \cdot C_X \cdot Z_F}. \quad (1)$$

A more advisable topology is the low Z_{in} transimpedance amplifier given in Fig. 1(b), because it fixes the voltage of the electrode to virtual ground, ensuring low voltages at the circuit's nodes. Although the transference function (2) also depends on the capacitance C_X , it is a linear dependence that admits online calibration

$$V_O(s) = -V_X(s) \cdot s \cdot C_X \cdot Z_F. \quad (2)$$

This paper, intended for power-line voltage measurements, is based on a low Z_{in} transimpedance amplifier with self-calibration of the coupling capacitance C_X proposed by Livobe and Singer [11]. The only practical implementation of this kind of NCVM system reported in literature [12] digitizes the analog output and performs a power spectral analysis to estimate the rms value of v_X . Nevertheless, no experimental results of arbitrary waveform signals measurements were reported, as it was for other methods [9], [10] which have not self-calibrated the scale factor and requires human intervention on each measure to calibrate the coupling capacitance.

This paper presents a quantitative noise and uncertainty analysis to identify the different constraints of the technique,

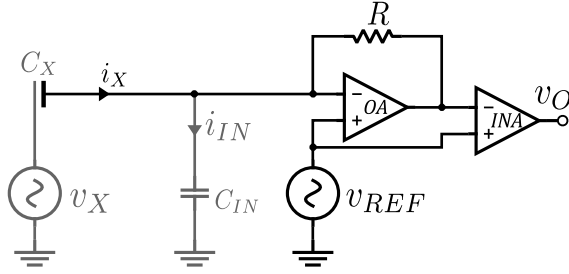


Fig. 2. Simplified scheme of analog front end used by NCVM method, where C_X is the coupling capacitance and C_{in} represents the stray input capacitance of OA.

in order to extend the original system on [12] to measure arbitrary waveform voltages.

II. NCVM METHOD FUNDAMENTALS

The NCVM system reported in this paper is based on the method patented by Libove and Singer [11]. It allows the measurement of an unknown voltage v_X on an isolated conductor placing an electrode in its vicinity, thus coupling it through a small and unknown capacitance C_X , through which a displacement current i_X flows. This current is processed by the circuit, shown in Fig. 2, which provides an output voltage v_O proportional to the derivatives of v_X and the reference voltage v_{REF} used for self-calibration. The output signal v_O is further processed to obtain \hat{v}_X : a time domain estimation of v_X .

A. Circuit Operation

The output voltage v_O in Fig. 2 can be expressed in the Laplace domain as

$$V_O(s) = \underbrace{s \cdot G_X \cdot V_X(s)}_{V_{O,X}(s)} + \underbrace{(-s(G_X + G_{in}))V_{REF}(s)}_{V_{O,REF}(s)} \quad (3)$$

where the factors G_X and G_{in} are defined as

$$G_X = C_X \cdot R \cdot G_{INA} \quad (4)$$

$$G_{in} = C_{in} \cdot R \cdot G_{INA}. \quad (5)$$

In (5), C_{in} represents the input capacitance of the operational amplifier (OA) that is neglected on the original patent, but is of main concern in real circuits as was pointed out in [12]. G_{INA} is the gain of the instrumentation amplifier (INA) that subtracts the signal v_{REF} from the OA's output.

From (3), two transfer functions $T_X(s)$ and $T_{REF}(s)$ can be defined

$$T_X(s) = \frac{V_{O,X}(s)}{V_X(s)} = s \cdot G_X \quad (6)$$

$$T_{REF}(s) = \frac{V_{O,REF}(s)}{V_{REF}(s)} = -s(G_X + G_{in}). \quad (7)$$

To obtain the estimation \hat{v}_X , the NCVM method must separate $v_{O,X}$ from $v_{O,REF}$, and pass it through the inverse transference function $T_X^{-1}(s) = (s \cdot G_X)^{-1}$. This implies the integration of $v_{O,X}$ and its scaling by G_X^{-1} .

As can be seen in (4), the factor G_X depends on the unknown capacitance C_X but, as it will be shown later, it can be estimated from $v_{O,REF}$, thus providing a self-calibration feature.

B. Self-Calibration Procedure

Given that the reference signal is a sinusoid with known amplitude V_{REF} and angular frequency ω_{REF} , $v_{O,REF}$ results a sinusoid with an amplitude V_{OREF} given as

$$V_{OREF} = V_{REF} \cdot \omega_{REF}(G_X + G_{in}) \quad (8)$$

that depends on C_X and also on C_{in} . The procedure proposed in [12] for disaffecting C_{in} in (8) to estimate G_X , consists in disconnecting the probe cable from the sensor (this implies $C_X = 0$) leading to a sinusoidal v_O signal with an amplitude V_{OREF}^{CAL} , given in the following equation:

$$V_{OREF}^{CAL} = V_{REF} \cdot \omega_{REF} \cdot G_{in}. \quad (9)$$

By this way, measuring V_{OREF}^{CAL} a single time, and computing V_{OREF} while acquiring v_X , the scale factor G_X can be computed online as

$$\hat{G}_X = \frac{\hat{V}_{OREF} - \hat{V}_{OREF}^{CAL}}{V_{REF} \cdot \omega_{REF}} \quad (10)$$

where the hat mark ($\hat{\cdot}$) denotes estimated or computed quantities.

Thus, the complete implementation of the method requires first a single-time estimation of the sinusoid amplitude \hat{V}_{OREF}^{CAL} during which the electrode cable must be disconnected, and then, during the measurement of v_X .

- 1) Separate v_O into $v_{O,X}$ and $v_{O,REF}$ by filtering.
- 2) Estimate \hat{V}_{OREF} from $v_{O,REF}$.
- 3) Compute \hat{G}_X using (10).
- 4) Estimate v_X integrating $v_{O,X}$ and scaling by \hat{G}_X^{-1} .

Although in the original patent [11] a complex analog signal processing is suggested, a simpler way to perform these tasks is by digital signal processing.

Note that ω_{REF} must be carefully chosen, because if the amplitude spectrum of v_X has components in ω_{REF} , v_O cannot be separated correctly into $v_{O,X}$ and $v_{O,REF}$, and the autocalibration scheme does not work properly. Other contributions not correlated with V_{REF} can be eliminated by the use of coherent averaging.

C. Shielding

The coupling capacitance C_X can be very small (1–5 pF) and also the current i_X that flows through it. To avoid other currents than i_X from reaching the electrode's cable (hence be amplified as i_X is), a coaxial cable must be used to link the electrode with the amplifier. The inner conductor is connected to the electrode plate and the outer shield is driven by v_{REF} and connected to the conductive shield case that surrounds the electrode (Fig. 3). Because of the "virtual ground approximation," ideally both conductors (the electrode and its driven shield) are at the same potential and no current flows through the shield capacitance C_{SH} . Nevertheless, as it will be analyzed further on, the limited OA's open-loop gain combined with high values of C_{SH} may introduce measurements errors. The value of C_{SH} , which depends on the length of the coaxial cable, and on the separation between the shielding and the electrode, can be up to hundreds of picofarad. The measured value of the built prototype is $C_{SH} \approx 100$ pF.

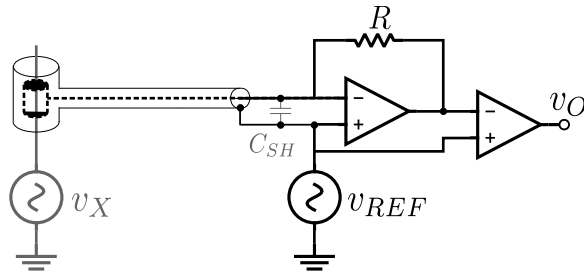


Fig. 3. Scheme of analog front end with a cylindrical electrode probe, surrounded by a guarded shield connected to v_{REF} to reject interference currents, where C_{SH} represents the stray capacitance between electrode and shield.

III. UNCERTAINTIES ANALYSIS

The signal v_X is not directly measured but computed through a processing algorithm which involves estimated quantities as the sinusoid amplitudes \hat{V}_{OREF} and \hat{V}_{OREF}^{CAL} . In fact, the estimation \hat{v}_X is obtained by passing the measured signal $v_{O,X}$ through a supposed inverse transference function $T_X^{-1}(s)$ implemented as an integrator, and then scaled by the inverse of the estimated gain \hat{G}_X computed by (10). The Laplace transform $\hat{V}_X(s)$ of the estimation of v_X is given as

$$\begin{aligned}\hat{V}_X(s) &= T_X^{-1}(s) \cdot V_{O,X}(s) = T_X^{-1}(s) \cdot T_X(s) \cdot V_X(s) \\ &= \frac{1}{s \cdot \hat{G}_X} \cdot s \cdot G_X \cdot V_X(s) = \frac{1}{\hat{G}_X} \cdot G_X \cdot V_X(s) \\ &= \frac{\omega_{REF} \cdot V_{REF}}{\hat{V}_{OREF} - \hat{V}_{OREF}^{CAL}} \cdot G_{INA} \cdot R \cdot C_X \cdot V_X(s).\end{aligned}\quad (11)$$

Several factors affect the relationship between $\hat{V}_X(s)$ and $V_X(s)$ given by (11), leading to an estimation error $\Delta v_X = \hat{v}_X - v_X$ which can be expressed as a relative error

$$e_{v_X} = \frac{\Delta v_X}{v_X} = \frac{\omega_{REF} \cdot V_{REF} \cdot G_{INA} \cdot R \cdot C_X}{\hat{V}_{OREF} - \hat{V}_{OREF}^{CAL}} - 1.\quad (12)$$

These sources of measurement uncertainties are analyzed in the following paragraphs. The noise generated by the circuit's components which adds a random error to each estimated sample of \hat{v}_X is analyzed in Section IV.

A. Estimation Errors for \hat{V}_{OREF} and \hat{V}_{OREF}^{CAL}

The amplitude estimations of both sinusoids at frequency ω_{REF} are carried out by the Fourier analysis of v_O signal. Additive random noise and other uncorrelated signals lead to random estimation errors $\pm \Delta V_{OREF}$ and $\pm \Delta V_{OREF}^{CAL}$ that are proportional to the inverse square root of the number of samples used for the estimation [13]. Therefore, these errors can be reduced arbitrarily if estimations \hat{V}_{OREF} and \hat{V}_{OREF}^{CAL} are done using a large enough time window.

B. Variations of Circuit Parameters Over Time

In the original version of method [11], C_{in} introduces a systematic error that the initial calibration step proposed in [12] disaffects. However, during long-term measurements, it is highly probably that the value of C_{in} will depart from its value at the initial calibration step (C_{in}^{CAL}), for example,

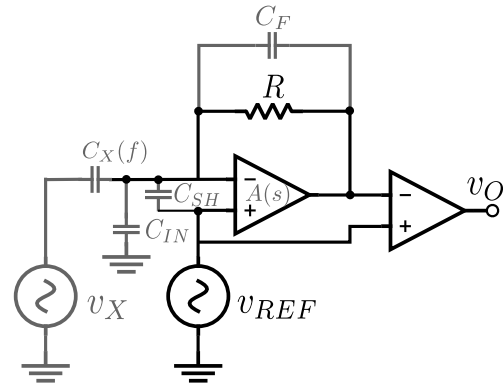


Fig. 4. Schematic showing finite OA open-loop gain $A(s)$, stray capacitances C_F and C_{SH} , and frequency-dependent electrode capacitance $C_X(f)$.

due to temperature effects. The same can happen with the rest of the parameters involved in the value of \hat{V}_{OREF}^{CAL} in (9) as: R , G_{INA} , V_{REF} , and ω_{REF} . This can be seen as an error in the calibration step

$$\Delta V_{OREF}^{CAL} = V_{OREF}^{CAL} - \hat{V}_{OREF}^{CAL}\quad (13)$$

where \hat{V}_{OREF}^{CAL} is the estimated value at initial calibration, used for calculations, and V_{OREF}^{CAL} is the current value. As it will be described in Section V-D, the variation of $(\Delta V_{OREF}^{CAL}/V_{OREF}^{CAL})/\Delta T$ could be of around $-0.2\%/^{\circ}\text{C}$.

This kind of error can be minimized by means of periodic "initial" calibrations, which require probe disconnection.

C. Frequency Dependence of C_X

The permittivity $\epsilon_R(f)$ of the cable sheath introduced in the probe varies with the frequency and the coupling capacitance C_X is confirmed by the air-dielectric capacitance in series with the sheath-dielectric capacitance. Therefore, the resultant value of capacitance C_X depends on frequency.

The NCVm method continuously (and indirectly) measures C_X by means of \hat{V}_{OREF} . Hence, any time variation of C_X is theoretically compensated. Nevertheless, this measurement is done at a fixed frequency f_{REF} , outside the frequency bandwidth of v_X , thus introducing an error given as

$$\Delta C_X = C_X - C_X(f_{REF})\quad (14)$$

where $C_X = C_X(f_X)$ is the coupling capacitance at signal bandwidth and $C_X(f_{REF})$ the coupling capacitance at reference frequency. This error ΔC_X depends on cable and probe materials, and also on probe geometry and relative position of the parts. For the experimental test described on Section V-E, the variation between $C_X(50\text{ Hz})$ and $C_X(f_{REF})$ resulted less than 2%.

D. Nonidealities of Circuit

Considering the circuit model of Fig. 4, which includes some additional effects such as the stray feedback capacitance C_F of about 1 pF, and the finite open-loop gain of the OA, $A(s) = (\omega_{GBP}/s)$, where ω_{GBP} is the gain-bandwidth product of the OA, the transference function results

$$T_X(s) = s \cdot G_X \left[\frac{1}{\left(1 + \frac{s}{\omega_F}\right) \left(1 + \frac{s}{\omega_{GBP}}\right) + \frac{s^2}{\omega_{GBP} \cdot \omega_{EQ}}} \right]\quad (15)$$

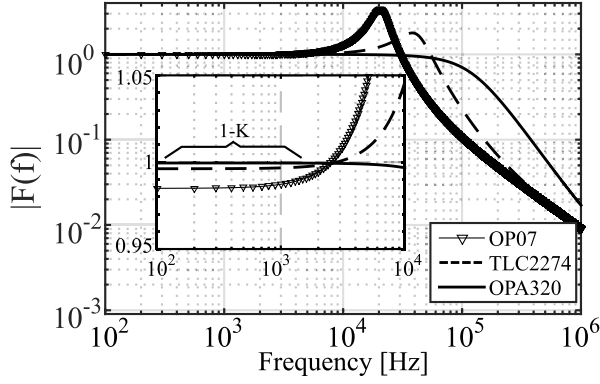


Fig. 5. Simulation of factor $|F(j.2\pi.f_{REF})|$ versus f_{REF} according (19), considering $R = 2.2 \text{ M}\Omega$, $C_X + C_{in} = 8 \text{ pF}$, $C_{SH} = 100 \text{ pF}$, $C_F = 1 \text{ pF}$, and three OAs with different values of ω_{GBP} : OP07 (0.6 MHz), TLC2274 (2.4 MHz), and OPA320 (20 MHz). The zoomed-in view region shows the approximation $F \approx 1 - K = 1 - (\omega_{GBP}R \cdot (C_X + C_{in}))^{-1}$.

where $\omega_F = (R \cdot C_F)^{-1}$, $\omega_{EQ} = (R \cdot C_{EQ})^{-1}$, and $C_{EQ} = C_X + C_{in} + C_{SH}$.

At low frequencies (below 1 kHz), the difference between (6) and (15) is negligible and (6) is still valid. Nevertheless, the denominator in (15) represents a second-order response that, if ω_{GBP} is not big enough, may have a resonance peak at

$$\omega_n = \sqrt{\omega_{GBP} \cdot \omega_{EQ}} = \sqrt{\frac{\omega_{GBP}}{R \cdot (C_{SH} + C_{in} + C_X)}} \quad (16)$$

with a damping factor

$$\zeta = \frac{1}{2} \cdot \left(\frac{1}{\omega_{GBP}} + \frac{1}{\omega_F} \right) \cdot \omega_n. \quad (17)$$

The transfer function $T_{REF}(s)$ becomes

$$T_{REF}(s) = -s \cdot (G_X + G_{in}) \cdot F(s) \quad (18)$$

where the factor $F(s)$ which concentrates the effects of the nonidealities of the circuit is given as

$$F(s) = \left[\frac{1 - \frac{1+s \cdot (\omega_{EQ}^{-1} + \omega_F^{-1})}{R \cdot (C_X + C_{in}) \cdot \omega_{GBP}}}{\left(1 + \frac{s}{\omega_F}\right) \left(1 + \frac{s}{\omega_{GBP}}\right) + \frac{s^2}{\omega_{GBP} \cdot \omega_{EQ}}} \right]. \quad (19)$$

The transference function (18) affects the estimations \hat{V}_{OREF} and \hat{V}_{OREF}^{CAL} , which are evaluated at $s = j\omega_{REF}$. Selecting an OA that leads to reasonable damping factor and using a ω_{REF} sufficiently lower than the natural frequency ω_n , then the factor in (19) can be simplified to $|F(j\omega_{REF})| \approx 1 - K$, with

$$K \approx (\omega_{GBP}R \cdot (C_X + C_{in}))^{-1}. \quad (20)$$

This factor represents a systematic error which can be disaffected.

The effect of the OA selection is illustrated in Fig. 5, where $|F(j \cdot 2\pi \cdot f_{REF})|$ versus f_{REF} was simulated considering $R = 2.2 \text{ M}\Omega$, $C_X + C_{in} = 8 \text{ pF}$, $C_{SH} = 100 \text{ pF}$, $C_F = 1 \text{ pF}$, and three OAs with different ω_{GBP} : OP07 (0.6 MHz), TLC2274 (2.4 MHz), and OPA320 (20 MHz). It is also depicted how the responses approximate to $1 - K$ at low frequencies ($\omega_{REF} \ll \omega_n$), where K is inversely proportional to the ω_{GBP} of the OA: 1.5% for OP07, 0.37% for TLC2274, and 0.05% for OPA320.

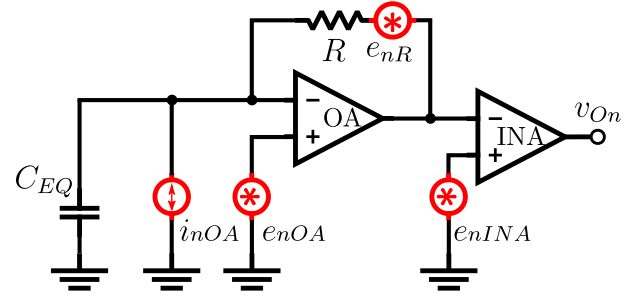


Fig. 6. Noise model for the analog front end showing the different noise sources.

E. Resultant Uncertainty on v_X

Based on the previous analysis, the estimation of sinusoidal amplitudes at the reference frequency is redefined in the following equations:

$$\hat{V}_{OREF}^{CAL} \approx V_{REF} \cdot \omega_{REF} \cdot C_{in} \cdot R \cdot G_{INA} \cdot (1 - K) - \Delta V_{OREF}^{CAL} \quad (21)$$

$$\hat{V}_{OREF} \approx V_{REF} \cdot \omega_{REF} (C_X(f_{REF}) + C_{in}) R \cdot G_{INA} \cdot (1 - K). \quad (22)$$

The general expression for the relative uncertainty e_{v_X} is shown in the following equation, which was obtained replacing (21) and (22) on (12) and using the definitions (13) and (14) for variations of V_{OREF}^{CAL} and C_X . Considering that these variations are much smaller than their nominal (or estimated) values: $\Delta C_X \ll C_X$ and $\Delta V_{OREF}^{CAL} \ll V_{OREF}^{CAL}$

$$e_{v_X} \approx e_{C_X} - \left(\frac{C_{in}}{C_X(f_{REF})} \right) \cdot e_{V_{OREF}^{CAL}} + K \quad (23)$$

where $e_{C_X} = (\Delta C_X / C_X(f_{REF}))$ and $e_{V_{OREF}^{CAL}} = (\Delta V_{OREF}^{CAL} / V_{OREF}^{CAL})$.

In (23), K can be disaffected or neglected if ω_{GBP} is high enough. About $e_{V_{OREF}^{CAL}}$, the corresponding error can be neglected in short-term measurements or with an automatic calibration procedure by using very low-stray capacitance switches.

Nevertheless, given that the probe is used with different kind of cables, e_{C_X} is difficult to predict. Furthermore, if v_X is not a narrowband signal, $C_X(f)$ will be nonconstant along the signal bandwidth. Thus, in general, e_{C_X} dominates on (23) calling for improvements on the probe geometry design to reduce the impact of cable sheath on C_X .

IV. RANDOM NOISE ANALYSIS

The estimation of steady-state voltage parameters, such as the rms value [12], allows the use of averaging to improve resolution at the expense of increasing the measurement time. This strategy is not feasible when instantaneous voltages like transient or arbitrary waveforms must be acquired, and resolution is limited by the instrumentation noise level.

Fig. 6 depicts the noise model for the analog front end of Fig. 2, which includes the main noise sources: the OA's input current and voltage noise sources i_{nOA} and e_{nOA} , the INA's input voltage noise source e_{nINA} , and the thermal noise of resistor R e_{nR} .

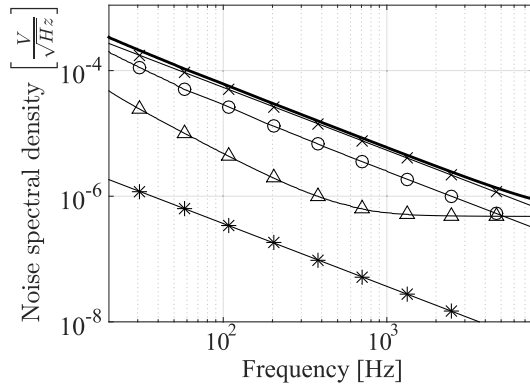


Fig. 7. Total noise spectral density and individual source contribution (RTI) for $R = 2.2 \text{ M}\Omega$, $C_X = 2.6 \text{ pF}$, $C_{EQ} \approx 100 \text{ pF}$, $I_{nOA} = 0.6 \text{ fA}/\sqrt{\text{Hz}}$, $E_{nOA} \approx 15 \text{ nV}/\sqrt{\text{Hz}}$, $E_{nINA} = 90 \text{ nV}/\sqrt{\text{Hz}}$, and $f_1 = 30 \text{ Hz}$. (—): total $V_{Xn}(f)$ computed by (25). (×): noise contribution of resistor R . (○): noise contribution of E_{nINA} . (△): noise contribution of E_{nOA} . (*): noise contribution of I_{nOA} .

Solving the circuit shown in Fig. 6, the noise spectral density $|V_{ON}(f)|^2$ of the output voltage v_O results

$$|V_{ON}(f)|^2 = G_{INA}^2 [|E_{nR}|^2 + |E_{nINA}(f)|^2 + |I_{nOA}(f)|^2 \cdot R^2 + |E_{nOA}(f)|^2 \cdot (1 + (2\pi f C_{EQ} R)^2)]. \quad (24)$$

Considering the transfer function (6), the referred-to-input (RTI) noise spectral density $|V_{Xn}(f)|^2$ is given as

$$|V_{Xn}(f)|^2 = \frac{1}{(2\pi f C_X)^2} \left[\frac{4kT}{R} + \frac{|E_{nINA}(f)|^2}{R^2} + |I_{nOA}(f)|^2 + \frac{|E_{nOA}(f)|^2}{R^2} \cdot (1 + (2\pi f C_{EQ} R)^2) \right] \quad (25)$$

where the resistor noise spectral density E_{nR} was replaced by the Nyquist expression [14].

Fig. 7 depicts the contribution of each noise source on Fig. 6 to the RTI noise spectral density $V_{Xn}(f)$ considering typical values for R and the capacitances involved. Note that E_{nOA} contribution is negligible below 10 kHz and also I_{nOA} (for FET input OA). $V_{Xn}(f)$ will be mainly determined by the noise of resistor R .

The rms value of the RTI noise, $V_{Xn,rms}$ is obtained by integration of (25) in the bandwidth of interest (f_1 to f_2) as

$$V_{Xn,rms} = \sqrt{\int_{f_1}^{f_2} |V_{Xn}(f)|^2 df}. \quad (26)$$

For a simplified analysis, considering that all noise sources have a flat spectrum and that f_2 is almost a decade greater than f_1 , $V_{Xn,rms}$ can be predicted by the following equation:

$$V_{Xn,rms} \approx \frac{1}{2\pi C_X \sqrt{f_1}} \sqrt{I_{nOA}^2 + \frac{4kT}{R} + \frac{E_{nINA}^2}{R^2}}. \quad (27)$$

As can be seen in (25) and (27), to reduce the noise the larger possible value of R and a low current noise OA (an FET input) are advisable. In addition, the value of G_{INA} does not influence the resultant noise value.

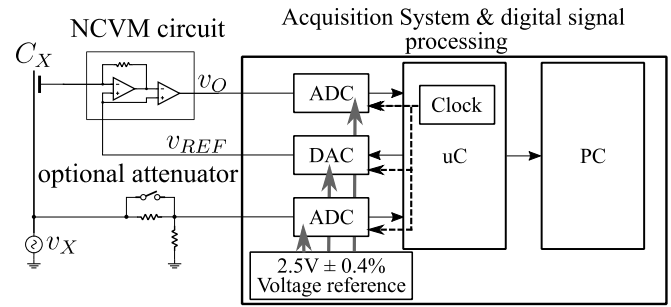


Fig. 8. Experimental setup to validate the NCV system for acquiring arbitrary signals.

The maximum practical value of resistor R is limited to avoid saturation effects at v_O . Considering power-line voltage monitoring, for a 220 V at 50-Hz system, the peak-to-peak voltage at v_O is approximately given as $V_{OPP} \approx 220.2\sqrt{2} \cdot 2\pi 50 C_X R$. Considering $C_X = 5 \text{ pF}$, a resistor R of around 2 MΩ keeps v_O below 2 V_{pp}.

Meanwhile, considering the use of an FET input OA and the INA111, with voltage noise source $E_{nINA} = 90 \text{ nV}/\sqrt{\text{Hz}}$, and $f_1 = 30 \text{ Hz}$, the effective RTI noise calculated by (27) results $V_{Xn,rms} \approx 0.6 \text{ mV}$. Even with coupling capacitances as low as $C_X = 1 \text{ pF}$, the noise results extremely lower than v_X ($V_{Xn,rms} \approx 3 \text{ mV}$) allowing the use of this NCV system to acquire power-line voltages and even volt-level arbitrary waveform signals.

V. NCV SYSTEM PROTOTYPE AND EXPERIMENTAL RESULTS

A prototype of the NCV system was constructed in order to acquire arbitrary waveforms and to validate the proposed models for noise and quantify errors.

The built electrode probe is similar to the probe reported in [12], made with two concentric pipes covered with conductive tape. The inner pipe (20 mm diameter–80 mm length) is the electrode plate and the outer pipe (30 mm diameter–140 mm length) is the shield that is driven by v_{REF} . The probe was connected to the analog front end by a 15-cm length coaxial cable (with its internal conductor connected to the electrode and the external one to the shield) which was terminated by a standard BNC connector to easily disconnect the probe for initial calibration.

The analog front end was implemented with the FET input OA TLC2274, an INA111 with $G_{INA} = 1$, and a resistor $R = 2.2 \text{ M}\Omega$.

To implement the digital signal processing of the NCV method, and also to obtain a quality measure of the estimated signal \hat{v}_X , the experimental setup of Fig. 8 was implemented. It has two high-resolution acquisition channels. Each channel has a single ADC (ADS1259) with more than 16 noise-free bits at 13.7 ksamples/s, which allows keeping quantization noise below the overall system noise (see Fig. 9). To achieve a good matching between channels, both ADCs share the same voltage reference of 2.5 V \pm 0.4% and also share the same external clock to allow synchronized sampling.

The first channel acquires the output v_O of the analog front end, while the second channel is used to acquire v_X directly.

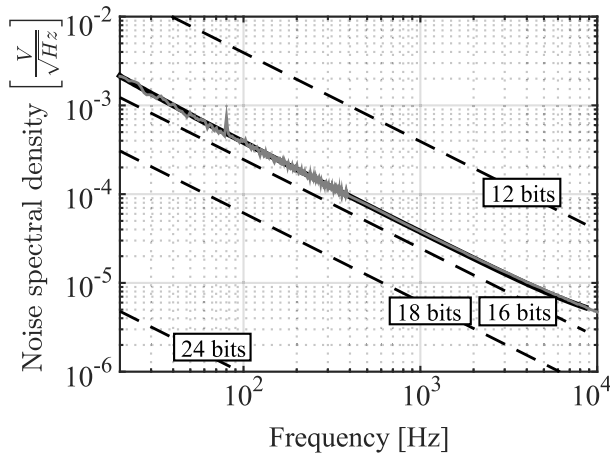


Fig. 9. Noise spectral density (RTI). Black solid line: predicted noise density by (25). Gray solid line: measured noise density. Dashed lines: equivalent RTI contribution for different ADC resolutions and sampling frequency $f_s = 13.7$ kHz.

An optional attenuator is used for conditioning high-voltage signals as power-line voltage. The second channel is required to compute the instantaneous error or deviation between \hat{v}_X , estimated with the NCVm technique, and v_X : $\Delta v_X = \hat{v}_X - v_X$. The instantaneous amplitude and the rms value of Δv_X are used as performance metrics.

For such comparative analysis, the absolute accuracy of the ADCs is not as significant as their matching is. The error between the two acquisition channels was verified applying a sinusoidal signal with variable frequency simultaneously to the input of both ADCs. The amplitudes of signals acquired by each channel differed by less than 0.025% in a frequency range from 10 Hz to 3 kHz. The amplitude of instantaneous error is also lower than 0.025% in a frequency range from 10 to 500 Hz. But due to a small delay of tens of nanoseconds between both channels, the amplitude of the error signal increases with frequency. Nevertheless, the error is kept below 0.15% for the complete 3 kHz bandwidth, which is suitable for the following experimental tests.

The sinusoid v_{REF} (with amplitude $V_{REF} \approx 1$ V and frequency $f_{REF} = 1.37$ kHz) is generated synchronously with the sampling frequency of ADCs. So that a whole number of samples (ten) are taken on each period of v_{REF} , simplifying the computation of \hat{V}_{OREF} . The generation of v_{REF} and all further signal processing of the NCVm method (filtering, integration, and scaling) is performed in real time by an ARM Cortex-M4F microcontroller from STMicroelectronics. The PC is only used for visualization and performance analysis.

A. Measurement of Analog Circuit's Noise Spectral Density

Noise spectral density at the output of the analog circuit $|V_{ON}(f)|$ was measured with a spectrum analyzer (Stanford Research System SR760). For this measurement a grounded cable was introduced on the probe (this implies $v_X = 0$) and v_{REF} was also grounded. Fig. 9 shows the measured output noise $|V_{ON}(f)|$ referred to the input denoted as $|V_{Xn}(f)|$. This experimental result shows a very good matching with the RTI noise predicted by (25), thus validating the proposed model.

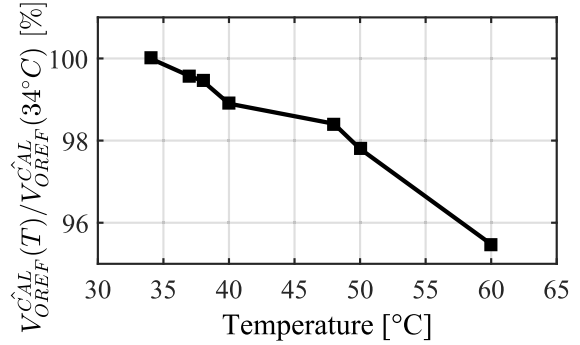


Fig. 10. Measure of $\hat{V}_{OREF}^{CAL}(T)$ relative to $\hat{V}_{OREF}^{CAL}(34^\circ\text{C})$.

B. Initial Calibration

In order to measure \hat{V}_{OREF}^{CAL} , necessary for computing \hat{G}_X by (10), the electrode's probe and its cable were detached from the input of the analog front end ($C_X = 0$). The obtained value was $\hat{V}_{OREF}^{CAL} = 101.3$ mV, which yields $C_{in}^{CAL} \approx 5.25$ pF.

C. Measurement of Noncontact System's RMS Noise

Connecting the electrode probe with $v_X = 0$, the component at f_{REF} was $V_{OREF} = 151.4$ mV ($C_X(f_{REF}) \approx 2.6$ pF) resulting in $\hat{G}_X = 1.71 \times 10^5$ s. After integration, scaling by \hat{G}_X^{-1} and filtering from 30 Hz to 3 kHz (-3 -dB bandwidth), the overall rms noise was $V_{Xn,rms} = 1.6$ mV, while the rms noise predicted by (27) is 1.2 mV.

D. Measurements of $e_{V_{OREF}^{CAL}}$

In order to verify the analysis of Section III-B, a test measuring \hat{V}_{OREF}^{CAL} for 30 min was made, with the probe disconnected and with a temperature sensor touching the printed circuit board (PCB). No variation of the measured value was observed.

On a second test, \hat{V}_{OREF}^{CAL} was also measured but at different temperatures. To change the temperature, the controlled heating airflow of a soldering station was directed to the OA until the measured temperature is stabilized.

The experiment results are depicted on Fig. 10, showing an average decrement of \hat{V}_{OREF}^{CAL} with temperature of $e_{V_{OREF}^{CAL}}/\Delta T \approx -0.2$ %/°C.

E. Measurements of Frequency Dependence of C_X

For the evaluation of the frequency dependence of C_X , a frequency sweep was performed using a 1.5-V amplitude sinusoidal source v_X . This signal was estimated by the NCVm technique and simultaneously acquired directly by the second channel. This last channel was used to verify the actual v_X amplitude and to compute e_{v_X} for each frequency, to obtain $e_{C_X}(f) = e_{v_X}(f) - e_{v_X}(\approx f_{REF})$.

The cable at v_X potential introduced in the probe had a 10 mm² Cooper section, and was protected by a 1-mm thickness polyvinyl chloride (PVC) sheath.

A maximum error $e_{C_X} = 2\%$ was observed for the lower frequency (35 Hz), and it decreases when frequency approached to f_{REF} , where $C_X(f_{REF}) = 5.02$ pF.

Stripping the cable and repeating the measurement with the cable in the same position, the maximum error was

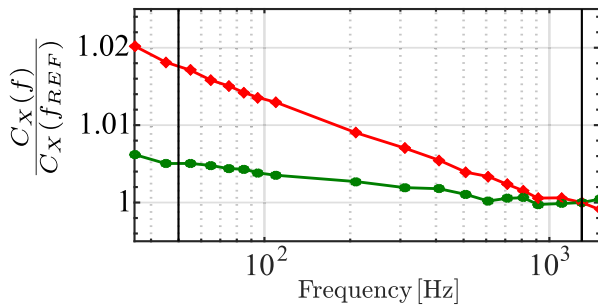


Fig. 11. Variation of $C_X(f)$ relative to $C_X(1.3 \text{ kHz})$. (\diamond): sheathed cable. (\bullet): unsheathed cable. Vertical solid lines: $f_{\text{REF}} = 1.3 \text{ kHz}$ and 50 Hz (power-line frequency).

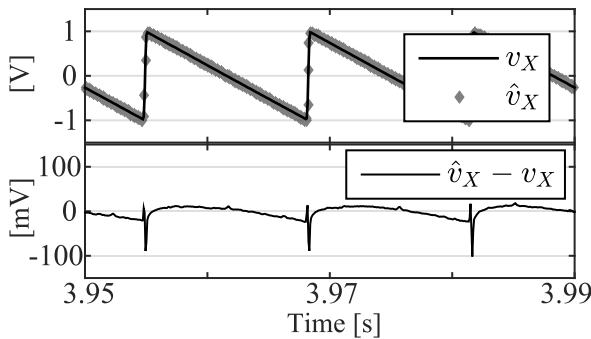


Fig. 12. Evaluation of NCVM system acquiring a $2 \text{ V}_{\text{pp}}-75 \text{ Hz}$ sawtooth signal.

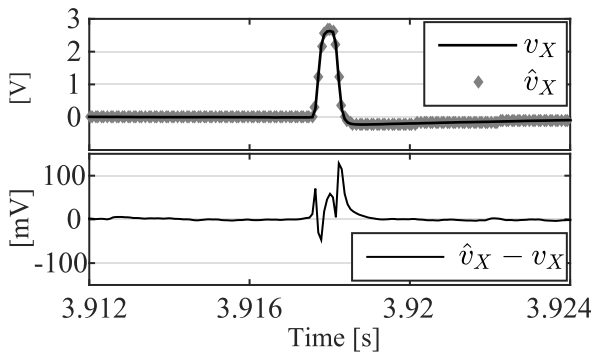


Fig. 13. Evaluation of NCVM system acquiring a $2.5 \text{ V}-500 \mu\text{s}$ pulse transient signal.

$e_{C_X} = 0.6\%$ and $C_X(f_{\text{REF}}) = 3.85 \text{ pF}$ (this variation was presumably due to the thin PVC tube that supported the electrode). Fig. 11 illustrates the variation of \hat{v}_X with frequency for both cases.

F. Measurement of Arbitrary Waveform Signals

In order to evaluate the ability of the NCVM system for acquiring arbitrary waveform signals, two different signal sources were used as v_X : a laboratory signal generator and a power-line (220 V at 50 Hz) “hot” conductor. In the latter case, an attenuator was used in the second channel input.

Figs. 12 and 13 show the comparison between v_X and its estimation \hat{v}_X provided by the NCVM system. They also show the error signal computed as the difference $\hat{v}_X - v_X$. For the chosen signals (sawtooth and rectangular pulse transient), the instantaneous value estimated by the NCVM system has a very small deviation ($1-100 \text{ mV}$) relative to instantaneous

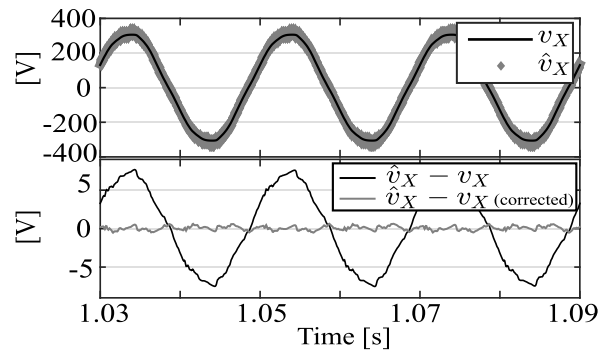


Fig. 14. Evaluation of NCVM system acquiring power-line voltage ($220 \text{ V}_{\text{rms}} - 50 \text{ Hz}$).

values of the input signal. The worst cases are the abrupt slopes, composed by high-frequency components that are slightly distorted, while for smooth signal segments, the instantaneous error is less than 10 mV .

Fig. 14 depicts the comparison between direct and noncontact power-line voltage measurements, showing, as on previous measurements, a very good matching. Nevertheless, because of the PVC sheathed cable, $e_{C_X} \approx 2.2\%$ at mains frequency (50 Hz), and the instantaneous error is up to 7 V (5 V_{rms}). Correcting this scale error (multiplying \hat{v}_X by 0.978), the instantaneous error, which is also shown in Fig. 14, decreases to less than 0.6 V . The effective voltage of the error after manual correction is $0.28 \text{ V}_{\text{rms}}$, which is 0.12% of the power-line effective voltage. This residual error is a combination of a frequency-dependent coupling capacitance C_X and experimental errors due to attenuator and low-pass filtering effects.

Note also that for all plots, no delay was applied to any signal, because the NCVM method preserves not only the amplitude but also the phase information. This nontrivial feature means that this method is well suited to perform noncontact power measurements.

VI. CONCLUSION

An NCVM technique with scale factor self-calibration, intended for measurement of steady-state rms voltages [11], [12] was extended to acquire high-quality transient and arbitrary waveforms. This means an improvement against other NCVM techniques [9] which are able to measure arbitrary signal waveforms but still need complex or nonautomated procedures to calibrate the coupling capacitance C_X .

To predict the accuracy and the constraints of the NCVM method, a noise voltage model was proposed and validated by experimental results. The conclusion is that using values for the resistor gain R (see Fig. 2) greater than $500 \text{ k}\Omega$, and an FET input OA, the expected rms noise of \hat{v}_X , over a 3-kHz bandwidth, is below 10 mV . The noise level is reduced as R increases, but this also reduces the input voltage range of v_X . In order to measure power-line voltages, with maximum coupling capacitances of $C_X \approx 5 \text{ pF}$, practical values for R must be below $5 \text{ M}\Omega$ to avoid saturation.

Other aspects of circuit design to pay attention to are the selection of OAs with a high ω_{GBP} and to keep low-stray shield capacitance C_{SH} values (short coaxial electrode cable

and careful probe design). Nevertheless, the main issue of the NCVM is the error introduced by the frequency-dependent permittivity of cable sheath, which impacts on C_X . This issue calls for further investigation on probe design to achieve a C_X value insensitive to cable sheath material.

The reported experimental results validate the previous analyses and show the feasibility of the measurement method to acquire arbitrary waveform voltage signals without contact. As a paradigmatic example of application of this technique, the contactless measurement of power-line voltage is accomplished with an error of 2.2% in a 3-kHz bandwidth using the self-calibration feature and an error of 0.12% after manual adjustment.

Because the NCVM method preserves not only the amplitude but also the phase information, it is well suited to combine with other well-known techniques for contactless current measurement to perform the noncontact measurements of power consumption.

ACKNOWLEDGMENT

The authors would like to thank S. Rodriguez for his help with PCBs manufacture and also F. N. Guerrero for his advice on paper writing.

REFERENCES

- [1] J. S. Bobowski, M. S. Ferdous, and T. Johnson, "Calibrated single-contact voltage sensor for high-voltage monitoring applications," *IEEE Trans. Instrum. Meas.*, vol. 64, no. 4, pp. 923–934, Apr. 2015.
- [2] L. Wu, P. A. A. F. Wouters, E. J. M. van Heesch, and E. F. Steennis, "On-site voltage measurement with capacitive sensors on high voltage systems," in *Proc. IEEE Trondheim PowerTech (POWERTECH)*, Jun. 2011, pp. 1–6.
- [3] I. A. Metwally, "D-dot probe for fast-front high-voltage measurement," *IEEE Trans. Instrum. Meas.*, vol. 59, no. 8, pp. 2211–2219, Aug. 2010.
- [4] D. Grant, G. Hearn, W. Maggs, and I. Gonzalez, "An electrostatic charge meter using a microcontroller offers advanced features and easier ATEX certification," *J. Electrostat.*, vol. 67, nos. 2–3, pp. 473–476, 2009. [Online]. Available: <http://www.sciencedirect.com/science/article/pii/S0304388609000564>
- [5] Y. Hu, Y. Yan, L. Wang, X. Qian, and X. Wang, "Simultaneous measurement of belt speed and vibration through electrostatic sensing and data fusion," *IEEE Trans. Instrum. Meas.*, vol. 65, no. 5, pp. 1130–1138, May 2016.
- [6] Y.-C. Chen, B.-S. Lin, and J.-S. Pan, "Novel noncontact dry electrode with adaptive mechanical design for measuring EEG in a hairy site," *IEEE Trans. Instrum. Meas.*, vol. 64, no. 12, pp. 3361–3368, Dec. 2015.
- [7] E. Spinelli and M. Haberman, "Insulating electrodes: A review on biopotential front ends for dielectric skin–electrode interfaces," *Physiol. Meas.*, vol. 31, no. 10, pp. S183–S198, Oct. 2010. [Online]. Available: <http://www.ncbi.nlm.nih.gov/pubmed/20834109>
- [8] G. McKenzie and P. Record, "Non-contact measurement of dc voltages using nonlinear elements," *Meas. Sci. Technol.*, vol. 23, no. 4, p. 045001, 2012.
- [9] D. Lawrence, J. S. Donnal, S. Leeb, and Y. He, "Non-contact measurement of line voltage," *IEEE Sensors J.*, vol. 16, no. 24, pp. 8990–8997, Dec. 2016.
- [10] D. Balsamo, D. Porcarelli, L. Benini, and B. Davide, "A new non-invasive voltage measurement method for wireless analysis of electrical parameters and power quality," in *Proc. IEEE SENSORS*, Nov. 2013, pp. 1–4.
- [11] J. M. Libove and J. R. Singer, "Apparatus for measuring voltages and currents using non-contacting sensors," U.S. Patent 5473244, Dec. 5, 1995. [Online]. Available: <https://www.google.com/patents/US5473244>
- [12] P. S. Shenil, R. Arjun, and B. George, "Feasibility study of a non-contact ac voltage measurement system," in *Proc. IEEE Int. Instrum. Meas. Technol. Conf. (I2MTC)*, May 2015, pp. 399–404.
- [13] S. M. Kay, *Fundamentals of Statistical Signal Processing: Estimation Theory*, vol. 1. Upper Saddle River, NJ, USA: Prentice-Hall, 1993.
- [14] H. Nyquist, "Thermal agitation of electric charge in conductors," *Phys. Rev.*, vol. 32, no. 1, pp. 110–113, Jul. 1928. [Online]. Available: <https://link.aps.org/doi/10.1103/PhysRev.32.110>



Marcelo Alejandro Haberman was born in La Plata, Argentina, in 1984. He received the Engineer degree in electronics and the Ph.D. degree from La Plata National University (UNLP), La Plata, in 2008 and 2016, respectively.

Since 2008, he has been with the Institute for Research in Electronics, Signal Processing, and Control (LEICI), UNLP, and the National Scientific and Technical Research Council (CONICET), La Plata, where he was involved in biopotential instrumentation and signal processing. He is currently a

Researcher with CONICET and a Teaching Assistant with the Engineering Department, UNLP. His current research interests include electronic instrumentation and signal processing.



Enrique Mario Spinelli was born in Balcarce, Argentina, in 1964. He received the Engineer degree in electronics and the M.S. and Ph.D. degrees from La Plata National University (UNLP), La Plata, Argentina, in 1989, 2000, and 2005, respectively.

Since 1990, he has been with the Institute of Industrial Electronics, Control, and Instrumentation (LEICI), UNLP, and the National Scientific and Technical Research Council (CONICET), La Plata, where he is currently a Professor of control systems with the Engineering Department, where he is

involved in scientific instrumentation. He is also a Researcher with CONICET. His current research interests include analog signal processing and biomedical instrumentation.